Functional form of the radiometric equation for the SNPP VIIRS reflective solar bands: an initial study

Ning Lei[1, *] and Xiaoxiong Xiong[2]

1. Science Systems and Applications, Inc., 10210 Greenbelt Road, Suite 600, Lanham, MD 20706 USA; ning.lei@ssaihq.com
2. Sciences and Exploration Directorate, NASA Goddard Space Flight Center, Greenbelt, MD, MD 20771 USA; xiaoxiong.xiong-1@nasa.gov

*** Author to whom correspondence should be addressed:** Tel: +1-301-867-2066

ABSTRACT

The Visible Infrared Imaging Radiometer Suite (VIIRS) aboard the Suomi National Polar-orbiting Partnership (SNPP) satellite is a passive scanning radiometer and an imager, observing radiative energy from the Earth in 22 spectral bands from 0.41 to 12 μm which include 14 reflective solar bands (RSBs). Extending the formula used by the Moderate Resolution Imaging Spectroradiometer instruments, currently the VIIRS determines the sensor aperture spectral radiance through a quadratic polynomial of its detector digital count. It has been known that for the RSBs the quadratic polynomial is not adequate in the design specified spectral radiance region and using a quadratic polynomial could drastically increase the errors in the polynomial coefficients, leading to possible large errors in the determined aperture spectral radiance. In addition, it is very desirable to be able to extend the radiance calculation formula to correctly retrieve the aperture spectral radiance with the level beyond the design specified range. In order to more accurately determine the aperture spectral radiance from the observed digital count, we examine a few polynomials of the detector digital count to calculate the sensor aperture spectral radiance.

Index Terms: SNPP VIIRS, radiometric calibration, solar diffuser, BRDF degradation, reflective solar bands, functional form

1. INTRODUCTION

For radiometric remote sensing sensors, it is fundamentally important to accurately calculate the sensor aperture spectral radiance from the background subtracted detector digital number commonly denoted as *dn*. For simplicity, simple polynomials of the *dn* are usually used to calculate the spectral radiance. For example, for the Moderate Resolution Imaging

Spectraradiometer (MODIS) instruments onboard the Aqua and Terra satellites, the aperture spectral radiance of the reflective solar bands (RSBs), is calculated by[1-2]

$$L = a_1 \times dn \quad . \tag{1}$$

For the Visible Infrared Imaging Radiometer Suite (VIIRS) on the Suomi National Polar-orbiting Partnership (SNPP) satellite, the spectral radiance is calculated by[3-5]

$$L = a_1 \times \left(c_0 + dn + c_2 \times dn^2\right) \tag{2}$$

where c_0 and c_2 are prelaunch determined.

The polynomial on the right hand side of Eq. (2) used by the VIIRS is meant to improve upon the formula used by the MODIS instruments. Although Eq. (2) may be a better choice than Eq. (1), our previous study[6] indicates inadequacy of the quadratic model for the RSBs over the design specified spectral radiance range. It is therefore very desirable to explore other functional forms of the *dn* to calculate the sensor aperture spectral radiance. It is also desirable to extend the functional forms of the *dn* to spectral radiances beyond the design specified range since many of the earth scenes are darker than the specified lower limits and some are brighter than the higher limits. Here, we evaluate the goodness of a few polynomial function forms of the *dn* and select the best one.

The data we use are from the prelaunch measurements with the SNPP VIIRS in a thermal vacuum chamber with the instrument temperature controlled at a constant. The radiance source is a Spherical Integrating Source with 100 cm in diameter (SIS-100) that is traceable to the National Institute of Standards and Technology reference. The SIS-100 was located outside the vacuum chamber and the radiation energy goes into the VIIRS through a glass window on the chamber. To assist finding a better functional form, first we need to identify the *dn* value needed for our calculation. Then we will rely on the statistical measure goodness-of-fit as well as visual inspections to identify a better model.

2. WHAT *dn* DO WE NEED?

The *dn* we need to enter a function to calculate the sensor aperture spectral radiance is the one purely from the photons emitted by the aperture scene, without temperature effects nor stray light. Mathematically, the digital count, denoted as the raw digital count is, when a detector in the VIIRS sensor sees a radiance source through the Earth View (EV) port

$$DN_{EV} = dn_{EV}(T_m)\left[1 + \alpha_T (T - T_m)\right] + dn_{\text{int}}(T_m)\left[1 + \beta_T (T - T_m)\right] + dn_{DCR} + dn_{s,EV} \quad . \tag{3}$$

In Eq. (3) dn_{EV} is the digital count purely from the aperture scene photons, T_m is the mean detector focal plane temperature, T is the focal plane temperature, α_T is the coefficient to account for the change in dn_{EV} due to focal plane temperature variation, dn_{int} is the digital count due to detector intricate electric current (with zero incident photon), β_T

is the coefficient to account for the change in dn_{int} due to focal plane temperature variation, dn_{DCR} is the digital count due to Digital Count Restore voltage, and $dn_{s,EV}$ is from photons outside of the aperture scene. Here we ignore any cross detector effects. What we want is $dn_{EV}(T_m)$.

To help find $dn_{EV}(T_m)$, we examine the digital count when the detector views the Space View (SV) port, expressed as

$$DN_{SV} = dn_{\text{int}}(T_m)\left[1+\beta_T(T-T_m)\right]+dn_{DCR}+dn_{s,SV}\ , \tag{4}$$

where similar to Eq. (3), $dn_{s,SV}$ is due to photons outside of the aperture scene. In establishing Eqs. (3) and (4), we use the approximation that the temperature dependence of the digital count is dominated by a linear dependence on the focal plane temperature, independent of the electronics temperature, demonstrated by Fig. 1. Fig. 1(a) shows in dots the SNPP DN_{SV}

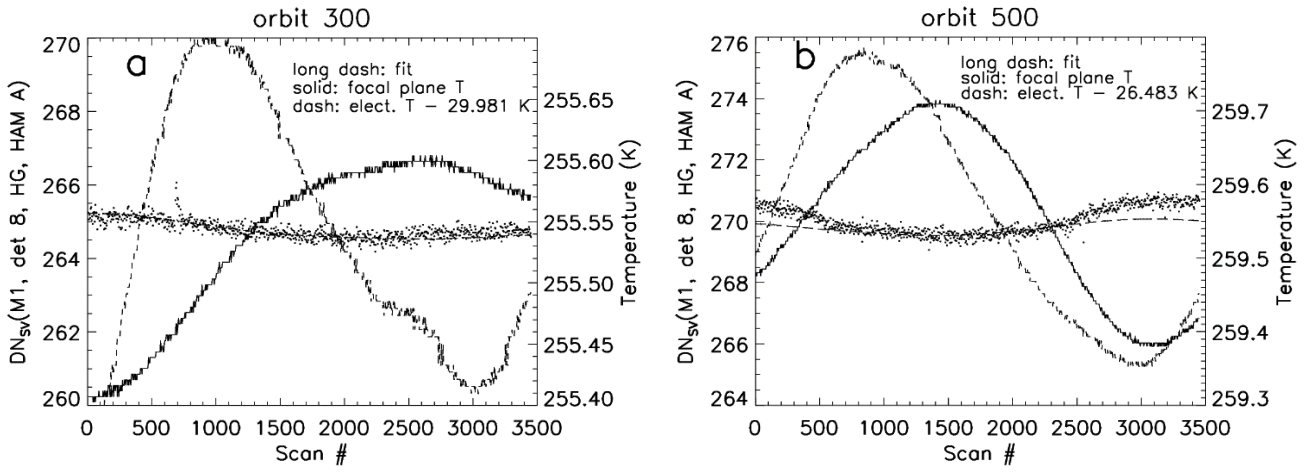

Figure 1. M1 band raw digital count when the SNPP VIIRS views the SV port, for the 8th detector at HAM side A and in the high-gain stage, from orbits (a) 300 and (b) 500.

versus the scan number (one scan lasts nominally 1.78 seconds) prior to NADIR door opening at satellite orbit 300, for the 8th detector of the M1 band at half-angle-mirror (HAM) side A and in the high-gain stage. The long dashed line is from the fit of a linear function of the VISNIR focal plane temperature to the DN_{SV} over scan numbers 1000 to 2000. Over these scan numbers the VIIRS sees the dark side of the Earth and the VIIRS itself is covered by the Earth shadow; essentially over these scans there is no stray light contamination (from this figure we can see that stray light contamination is small even when the VIIRS is hit by the solar radiation since the NADIR door was closed). Fig. 1(b) shows the DN_{SV} after the NADIR door opening at orbit 500. The figure demonstrates that when the earth reflected sunlight goes through the EV port, the stray light contribution to DN_{SV} is not zero, around 0.7 for the M1 band detector in the high-gain stage.

Fig. 1(b) also shows that over scan numbers from 2200 to 2300, the stray contamination over the SV port is nearly zero since the fit to the DN_{SV} over scan numbers from 1000 to 2000 traces well the DN_{SV} until the scan number is larger than 2300 (from scan numbers 700 to 2300, the fit traces the DN_{SV} well). Thus we conclude that *the stray light contamination over the senor solar diffuser (SD) observation that happens over scan numbers from 2200 to 2300 is also nearly zero, allowing for a clean on-orbit RSB radiometric calibration through observation of the sunlit SD*.

From Eqs. (3) and (4), we obtain

$$dn_{EV}(T_m) = \left[(DN_{EV} - DN_{SV}) + (dn_{s,EV} - dn_{s,SV})\right] \times \left[1 - \alpha_T (T - T_m)\right] \quad , \tag{5}$$

using that $1/\left[1 + \alpha_T (T - T_m)\right]$ is approximated by $1 - \alpha_T (T - T_m)$ since $\alpha_T (T - T_m)$ is much less than one. $dn_{s,EV}$ and $dn_{s,SV}$ have respective stray light contributions. Since the amount of stray light contribution is detector dependent, *if not taken into account, the stray light can create unwanted stripping for both the RSBs and the thermal emissive bands in terms of the retrieved earth scene spectral radiance. This unwanted stripping can be prominent if the far field scene has a high radiance level and the aperture radiance is low. Additionally, due to stray light contamination, simply using* $DN_{EV} - DN_{SV}$ *to determine sensor aperture spectral radiance can result in large relative errors*. These errors can persist, even after applying mathematical techniques to remove the unwanted striping. Consequently, we ask ourselves that under what conditions we can still use $DN_{EV} - DN_{SV}$ to correctly determine sensor aperture spectral radiance. One such condition is that the photons contributing to $DN_{EV} - DN_{SV}$ are from scenes of the same spectral radiance, namely both $dn_{s,SV}$ and $dn_{s,EV}$ are from scenes of the same spectral radiance. Under such condition, we can write $dn_{s,EV} = \alpha_{s,EV}\, dn_{EV}(T_m)$ and $dn_{s,SV} = \alpha_{s,SV}\, dn_{EV}(T_m)$. Realizing that $\alpha_T (T - T_m)$ is much less than one, we write Eq. (5) as

$$dn_{EV}(T_m) = \frac{(DN_{EV} - DN_{SV}) \times \left[1 - \alpha_T (T - T_m)\right]}{1 + \alpha_{s,EV} - \alpha_{s,SV}} \ . \tag{6}$$

Eq. (6) is approximately realized when the near field scene, including the aperture scene, has a spatially uniform high radiance level and the far field is relatively dark. The thermal vacuum tests through observing the SIS-100 is such a case when the source SIS-100 is relatively bright. The SIS-100, with a disk-like opening of a diameter of about 47 cm to allow light through, locates more than three meters away from the vacuum chamber window through which the VIIRS sees the source through the EV port. In this study, we use data from the nominal temperature plateau where the focal plane temperature was maintained to be very stable to be within a few dozen milliKelvins. Therefore the temperature dependence term in Eq. (6) is negligible, allowing us to approximate $dn_{EV}(T_m) = (DN_{EV} - DN_{SV})/(1 + \alpha_{s,EV} - \alpha_{s,SV})$ when DN_{EV} is relatively large. Consequently, a function of $DN_{EV} - DN_{SV}$ can be used to determine sensor aperture spectral radiance.

3. WHICH FUNCTIONAL FORM IS THE BEST?

In this study, the functional forms that we investigate are simple polynomials of the *dn*, with $dn = DN_{EV} - DN_{SV}$: $a_1 dn$, $a_1\left(c_0 + dn + c_2 dn^2\right)$, $a_1 dn\left(1 + c_2 dn\right)$, $a_1 dn\left(1 + c_2 dn + c_3 dn^2\right)$, and $a_1 dn\left(1 + c_2 dn + c_3 dn^2 + c_4 dn^3\right)$. The brightness of the SIS-100 was set through switching on and off the lamps inside. At each SIS-100 brightness level and gain stage, data were collected with an attenuator (a perforated plate) in and out of the optical path. For each of two attenuator positions, 50 scans were carried out (a scan means that the VIIRS telescope rotates one full turn). For each scan, the data taken at the EV port are from 120 consecutive equally separated angular positions, denoted as samples, for the M-bands, and 240 positions for the I-bands. The 120 samples (240 for the I-bands) aim at the central portion of the radiance source. There are 48 M-band samples for the SV port and 96 samples for the I-bands. The transmittance of the attenuator is assumed to be unchanged through the radiance levels. Denote $dn_{in} = DN_{EV} - DN_{SV}$ when the attenuator is in the optical path and $dn_{out} = DN_{EV} - DN_{SV}$ when the attenuator is out of the optical path, and τ as the transmittance, through adjusting the parameters in the function and τ we can minimize the difference between τ and $L_{ap}(dn_{in}; P) / L_{ap}(dn_{out}; P)$ over the source brightness levels in a least-squares sense, where *P* indicates the parameters and $L_{ap}(\ldots)$ indicates the aperture spectral radiance calculated through a functional form of *dn*. The source spectral radiance levels for the fit are taken to be within the design specified minimum and maximum values when the attenuator is out of the optical path after taking into account the transmittance of the glass window. We use the goodness-of-fits to evaluate the functional forms, as well as visual inspections.

To use the IDL curve fitting function mpcurvefit()[7], we need to have a function to predict something which can be directly measured, namely setting up an equation so that all model parameters are on the right hand side which gives the modeled value that can also be measured. For example, to use $a_1 \times dn\left(1 + c_2 \times dn + c_3 \times dn^2\right)$ as the functional form for the aperture spectral radiance, we first write

$$\tau = \frac{dn_{in}\left(1 + c_2 \times dn_{in} + c_3 \times dn_{in}^2\right)}{dn_{out}\left(1 + c_2 \times dn_{out} + c_3 \times dn_{out}^2\right)} , \tag{7}$$

and then from Eq. (7) we obtain

$$dn_{in} = \frac{\tau \times dn_{out}\left(1 + c_2 \times dn_{out} + c_3 \times dn_{out}^2\right)}{1 + c_2 \times dn_{in} + c_3 \times dn_{in}^2} . \tag{8}$$

Eq. (8) is different from the traditional one that has the format of $y = F(x; P)$ *where the x represents the independent variable and y the dependent variable. Eq. (8) has a format of* $y = F(x, y; P)$ *where y is both an independent and a*

dependent variable. $y = F(x, y; P)$ *significantly simplifies the procedure so that we can use mpcurvefit() to find P of any polynomials since there is no need to solve a polynomial equation like we did before*[5]. Solving a polynomial equation with an analytical expression higher than 4, in general, is impossible.

For each HAM side, there are 25 scans, corresponding to 25 data points at a particular sample position for the EV. We average the 25 DN_{EV} with a 3-sigma outlier rejection. DN_{SV} is the average from 48 samples (96 samples for the I-bands) per scan and then over the 25 scans. Our previous study[6] shows that the attenuator transmittance is slightly sample dependent. This dependence is expected since typically the holes in the attenuator allow different amount of photons (per unit time duration, per unit attenuator surface area, at the same source radiance level) to go through for photons traveling at different directions due to geometric shadowing. Consequently, we carry out our fits per sample across the source radiance levels. To avoid the adverse effect of the drifts in the source radiance level and the detector gain, at each source radiance setting and detector gain, data collection started with 50 scans with the attenuator out of the optical path and then two 50 scans with the attenuator in the path, followed by 50 scans with the attenuator out of the path. The time separation between the nearest 50-scan groups remains roughly a constant. Hence to remove the impact of the drifts, at each source radiance setting and detector gain and HAM side, we average the *dn* from the two attenuator-out scan groups and the attenuator-in scan groups, denoted as dn_{out} and dn_{in}, respectively. The dn_{out} and dn_{in} form a data point in our fitting procedure. Note that DN_{EV} is truncated to a 12-bit integer and DN_{SV} is a 14-bit number with 2 bits assigned for the

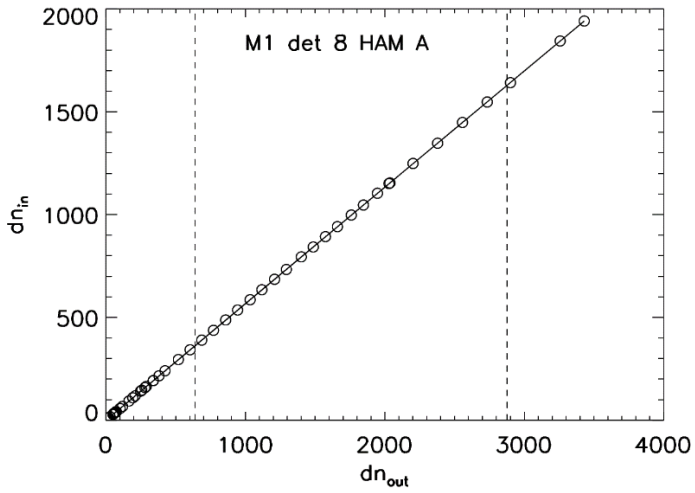

Figure 2. The measured and modeled dn_{in} versus the measured dn_{out} for the 8th detector of the M1 band at HAM side A and in the high-gain stage at the 60th sample position. The vertical dashed lines show the corresponding dn_{out} at the design specified minimum and maximum spectral radiances. The modeled dn_{in} is from Eq. (8).

fraction. The truncation of DN_{EV} creates a bias of 0.375. Hence, we add 0.375 to the measured DN_{EV}. In the fit, the weight for each data point is the inverse of the variance of the data point. The variance has contributions from both dn_{in} and dn_{out}, approximately given by, for the functional forms we consider in this study,

$\text{var}\left(dn_{in}\right)+\tau^2\ \text{var}\left(dn_{out}\right)-2\tau\times\text{covar}\left(dn_{in},dn_{out}\right)$. The covariance is essential zero because due to the average of the digital numbers in the attenuator position groups aforementioned, the source power and detector gain drift effect is removed. The variances has contributions from the noise among the digital numbers in the 25 scans and the noise in the source spectral radiance at the time duration that separates the nearest 50-scan groups. We add a signal quantization variance of 1/12+1/192 for the per scan *dn* to take care of the case when all the *dn* values in the 25 scans have the same number. We use a 6-sigma

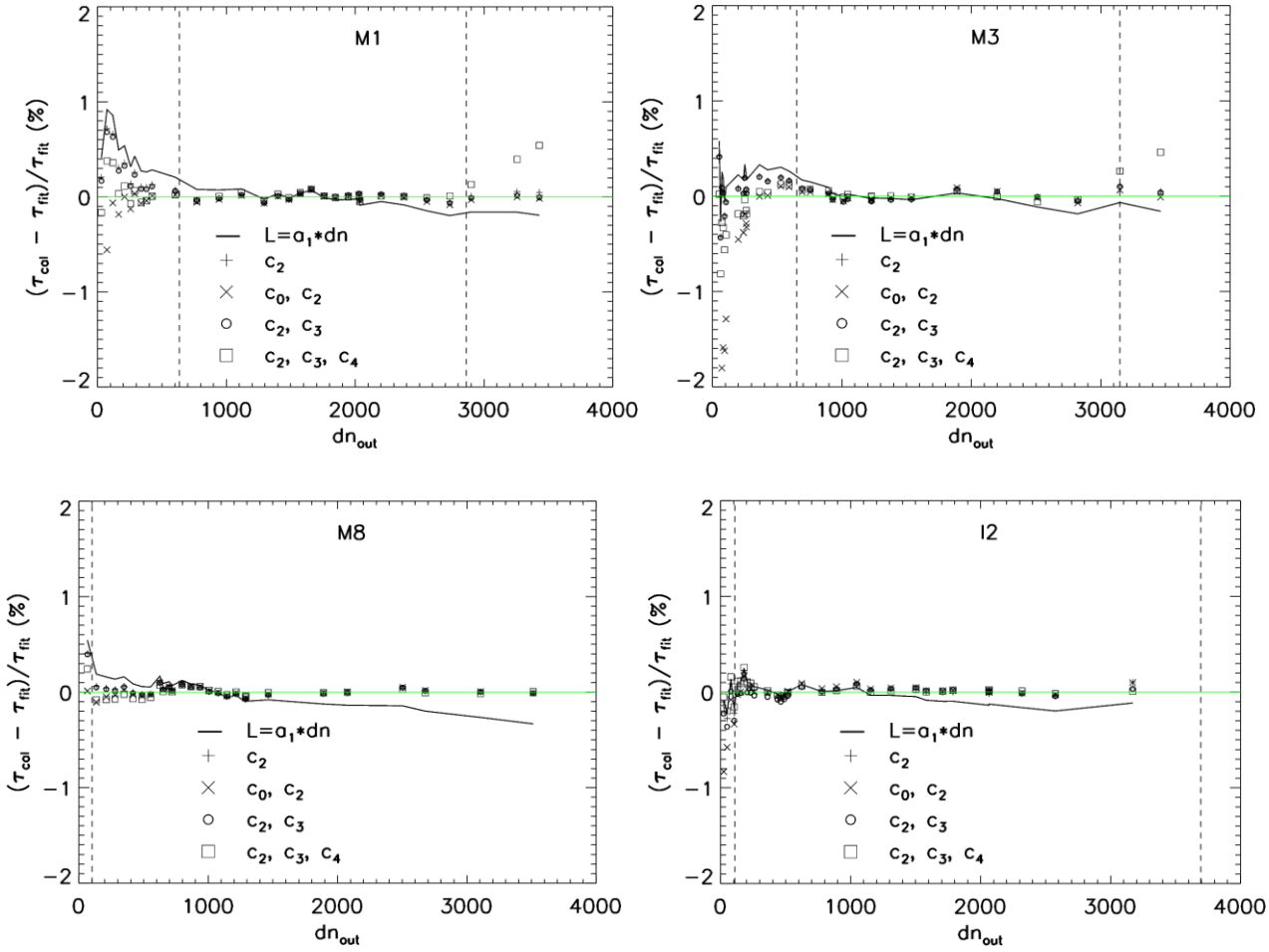

Figure 3. Relative difference between the attenuator transmittances calculated by the spectral radiance functional forms such as Eq. (7) and the one from the fitting process at HAM side A, averaged over 120 sample positions and 240 sample positions for the 8th detector of the M-bands and the 16th detector of the I-bands, respectively. The dn_{out} for the M-bands are for the 60th sample position in the high-gain stage and the average for the 119th and 120th positions for the I-bands. The vertical dashed lines indicate the dn_{out} corresponding to the design specified minimum and maximum spectral radiance levels.

outlier rejection in performing the fit. As an example, we show in Fig. 2 the measured dn_{in} versus the measured dn_{out} and the calculated one from Eq. (7) for the M1 band, the 8th detector, at HAM side A, and in high-gain stage, at the 60th sample position. The fit is carried out for data points between the two vertical dashed lines which show the corresponding dn_{out} at the design specified minimum and maximum spectral radiances. Visually, the fit is very good, even in the region

beyond the design specification. For each (band, detector, gain stage, HAM), the determined c-coefficients and a_1 are averaged over all sample positions, and for the *c*-coefficients additional average over the two HAM sides is performed.

The goodness-of-fit is obtained over the design specified spectral radiance region. The design specified spectral radiance region is for the case when the attenuator is out of the optical path. To simplify our visual examination, we only show the results for the mid-detector, namely, the 8th detector for the M-bands and the 16th detector for the I-bands, and in high-gain stage for dual-gain bands. The measure for the visual inspection is the attenuator transmittance relative difference between the fit obtained one and the one calculated from the measured dn_{in} and dn_{out} such as Eq. (7), averaged over the sample positions at HAM side A. In Fig. 3, we show the attenuator transmittance relative difference for the bands for which the goodness-of-fits (shown in Fig. 4) are significantly larger for the functional form of $L = dn \times \left(1 + c_2 \times dn + c_3 \times dn^2 + c_4 \times dn^3\right)$. Visual inspection of Fig. 3 indicates that among the functional forms the relative differences between $dn_{out}(\min)$ and $dn_{out}(\max)$ shown as the vertical dashed lines are similar, except $L = a_1 \times dn$. The functional form $L = a_1 \times dn$ performs the worst, often yielding a sloped attenuator transmittance relative difference. For the M8 and I2 bands, the maximum measured dn_{out} is well below $dn_{out}(\max)$ which is the dn_{out} calculated at the upper limit of the design spectral radiance. Not only we examine the transmittance relative difference between $dn_{out}(\min)$ and $dn_{out}(\max)$, we would also like to know the difference beyond the range of $[dn_{out}(\min), dn_{out}(\max)]$ since actual earth scene spectral radiance can be outside the design specified range. Below $dn_{out}(\min)$, for all bands none of the functional forms perform well, shown in Fig. 3, probably due to the effect of stray light so that we do not have a clean dn. At a radiance level below $L_{\min}$, the worst performer is $L = a_1 \times \left(c_0 + dn + c_2 \times dn^2\right)$, indicated by the crosses well below zero for the M3 and I2 bands. We expect that the stray light effect is more prominent at a lower *dn*. Beyond $dn_{out}(\max)$, the figures for the M3 and M8 bands show that $L = dn \times \left(1 + c_2 \times dn + c_3 \times dn^2 + c_4 \times dn^3\right)$ does not perform well since the transmittance relative difference is well away from zero, whereas other forms, except $L = a_1 \times dn$, perform similarly. As

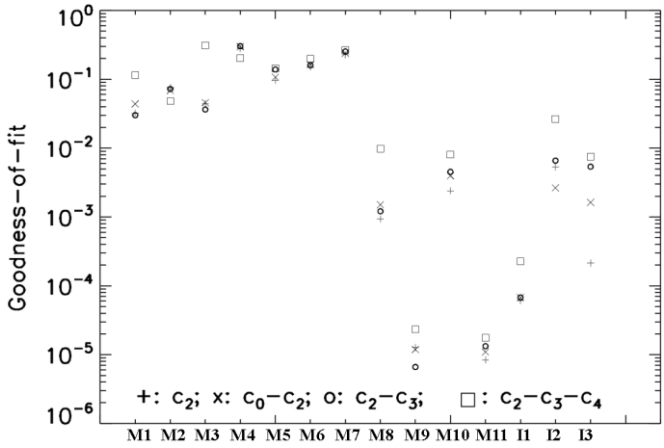

Figure 4. Goodness-of-fit for all RSBs, averaged over the detectors, sample positions, and HAM sides, and in the high-gain stage for the dual-gain bands.

a result, our visual examination of Fig. 3 favors $L = a_1 \times \left(dn + c_2 \times dn^2\right)$ and $L = a_1 \times \left(dn + c_2 \times dn^2 + c_3 \times dn^3\right)$. The poor performance for the quartic polynomial beyond $dn_{out}(\max)$ is due to input data inaccuracy, resulting inaccuracy in the c_4.

To distinguish the performances of $L = a_1 \times \left(dn + c_2 \times dn^2\right)$ and $L = a_1 \times \left(dn + c_2 \times dn^2 + c_3 \times dn^3\right)$, in Fig. 4 we plot the goodness-of-fit for each band, averaged over the sample positions, detectors, and HAM sides, in the high-gain stage for

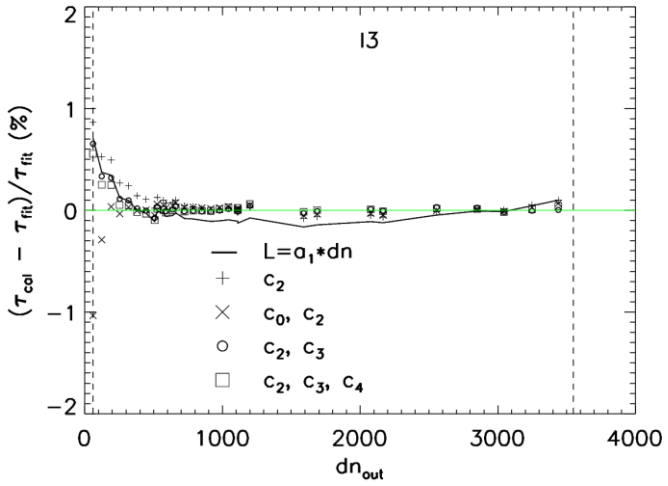

Figure 5. Relative difference between the attenuator transmittances calculated by the spectral radiance functional forms such as Eq. (7) and the one from the fitting process at HAM side A, for the 16th detector of the I3 band, averaged over 240 sample positions. The dn_{out} is the average for the 119th and 120th sample positions. The vertical dashed lines indicate the dn_{out} corresponding to the design specified minimum and maximum spectral radiance levels.

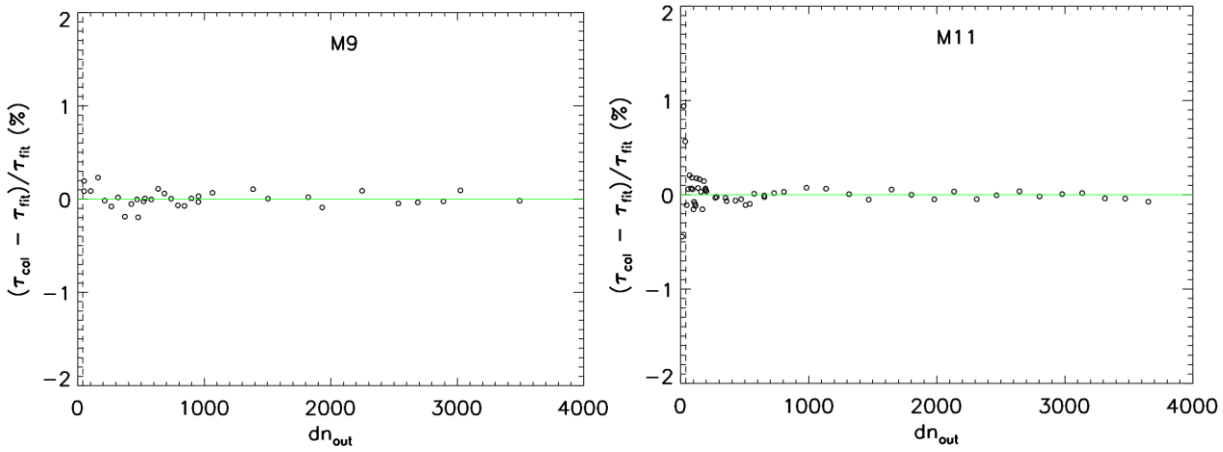

Figure 6. Relative difference between the attenuator transmittances calculated by the spectral radiance functional form $L = a_1 \times \left(dn + c_2 \times dn^2 + c_3 \times dn^3\right)$ and the one from the fitting process, averaged over both HAM sides and 120 sample positions, for the 8th detector of the M9 and M11 bands. The dn_{out} is for the 60th sample position at HAM side A. The vertical dashed line indicate the dn_{out} corresponding to the design specified minimum spectral radiance level. The dn_{out} corresponding to the design specified maximum spectral radiance level is beyond 4000.

the dual-gain bands. For the two polynomials, the goodness-of-fits are of very similar values for all the RSBs, except the I3 band. For the I3 band, $L = a_1 \times \left(dn + c_2 \times dn^2 + c_3 \times dn^3\right)$ yields a much larger goodness-of-fit value than $L = a_1 \times \left(dn + c_2 \times dn^2\right)$. Comparing with $L = a_1 \times \left(dn + c_2 \times dn^2 + c_3 \times dn^3\right)$, $L = a_1 \times \left(dn + c_2 \times dn^2\right)$ underperforms at

spectral radiances close to $L_{\min}$, shown in Fig. 5. As a result, we select $L = a_1 \times \left(dn + c_2 \times dn^2 + c_3 \times dn^3\right)$ as the best functional form.

For bands M9 and M11, the goodness-of-fit values are very low, shown in Fig. 4. This is due to poor fitting quality over low dn_{out} since the respective $dn_{out}(\min)$ is very low at about 40 for both bands. As an example, Fig. 6 shows the relative difference of the transmittances for the functional form $L = a_1 \times \left(dn + c_2 \times dn^2 + c_3 \times dn^3\right)$. This poor fitting quality is expected due to unknown stray light impact.

4. DISCUSSION

Over the design specified spectral radiance region of $[L_{\min}, L_{\max}]$, for the radiance functional forms that we study in this paper, in general the increase in the goodness-of-fit is associated with increasing polynomial order, shown in Fig. 4. Overall, $L = dn \times \left(1 + c_2 \times dn + c_3 \times dn^2 + c_4 \times dn^3\right)$ yields the largest goodness-of-fit values for the bands. This association indicates that we still do not have a true functional form to associate the *dn* with the sensor aperture spectral radiance, at least for some of the RSBs. The polynomials are simply the Taylor polynomial approximations to the unknown true functional form. Although in most cases the per sample based fitting process gives a goodness-of-fit value large enough to validate the model such as $L = dn \times \left(1 + c_2 \times dn + c_3 \times dn^2 + c_4 \times dn^3\right)$, once we average the values of the fit-determined

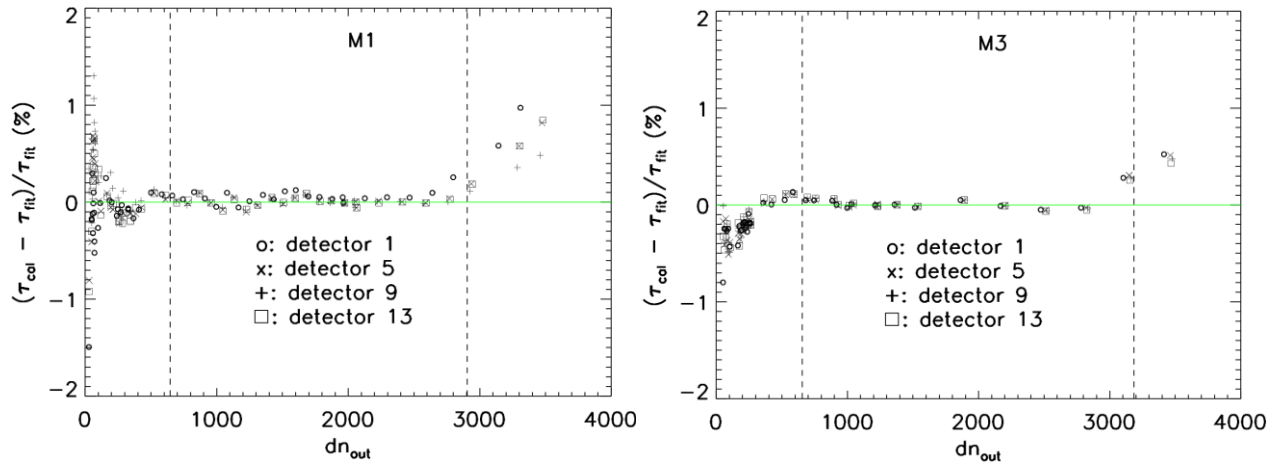

Figure 7. Relative difference between the attenuator transmittances calculated by the spectral radiance functional form such as Eq. (7) with $L = dn \times \left(1 + c_2 \times dn + c_3 \times dn^2 + c_4 \times dn^3\right)$ and the one from the fitting process, for the M1 and M3 bands, averaged over sample positions and HAM sides, in the high-gain stage for detectors 1, 5, 9, and 13 (detector numbers starts from 1). The dn_{out} is for the first detector at 60th sample position at HAM side A and in the high-gain stage. The vertical dashed lines indicate the dn_{out} corresponding to the design specified minimum and maximum spectral radiance levels.

polynomial coefficients over the sample positions, the goodness-of-fit with the averaged coefficients are much smaller, invaliding any of the models under study in this paper. This phenomenon is due to the systematic deviations between the attenuator transmittances from the fit and from the calculated such as by Eq. (7), and was demonstrated previously[6]. For

example, the systematic deviations in the region of $[dn_{out}(\min), dn_{out}(\max)]$ are clearly shown in Fig. 7. For detectors 1, 5, 9, and 13 in each of the M1 and M3 bands, the differences are nearly the same, indicating that the deviations from zero are not due to random noises. Note that the data in Fig. 7 are from applying $L = dn \times \left(1 + c_2 \times dn + c_3 \times dn^2 + c_4 \times dn^3\right)$. These systematic deviations indicate that $L = dn \times \left(1 + c_2 \times dn + c_3 \times dn^2 + c_4 \times dn^3\right)$ is not an adequate model over $[dn_{out}(\min), dn_{out}(\max)]$.

5. SUMMARY

In this study, for the SNPP VIIRS RSBs we have investigated the performances of a few polynomial functions that relate the background subtracted detector digital count *dn* to the sensor aperture spectral radiance. The functions which we have studied are $a_1 dn$, $a_1\left(c_0 + dn + c_2 dn^2\right)$, $a_1 dn\left(1 + c_2 dn\right)$, $a_1 dn\left(1 + c_2 dn + c_3 dn^2\right)$, and $a_1 dn\left(1 + c_2 dn + c_3 dn^2 + c_4 dn^3\right)$. Some of the functions are currently used by the MODIS and the SNPP VIIRS instruments. The study used the data collected with the SNPP VIIRS in a vacuum chamber at a constant temperature with an SIS-100 as the radiance source. To evaluate the performance of the functional forms, we pointed out that the *dn* should be purely due to the aperture radiance, meaning that when the aperture radiance is zero, we need to have a zero *dn*. More generally, we stated that the usefulness of using the *dn* to calculate the sensor aperture spectral radiance is under the condition of that the contribution to the *dn* is from a scene that has the same spectral radiance as the aperture scene. We showed the existence of stray light contamination due to earth reflected sunlight into the Earth View port and pointed out that a strong far field radiance source may introduce unwanted striping in the retrieved aperture scene spectral radiance, due to the stray light contamination non-uniformly distributed across the detectors. This striping could be especially visible if the aperture scene has low radiance levels. The contamination also introduces a bias in the retrieved aperture spectral radiance and a simple de-striping technique will not remove the bias. The SIS-100 is considered a nearly spatially uniform light source, allowing us to effectively evaluate the performance of the functional forms. The *DN* was collected with an attenuator placed in and out of the optical path. We assumed that the attenuator transmittance is unchanged over the source radiance levels and for each polynomial we established a simple relation of $dn_{in} = F\left(dn_{out}, dn_{in}; P\right)$, where *P* represents the polynomial coefficients and the attenuator transmittance that were determined by the fitting process. The data were collected over 120 and 240 consecutive angular positions denoted as the samples for the M- and I-bands, respectively, and for each attenuator position 50 scans were performed. The gains for the dual-gain bands were in the high-gain stage. We carried out least-squares fit for each detector at each sample position and each HAM side with a 6-sigma outlier rejection. The fit was carried out over the design spectral radiance range for the case when the attenuator is out of the optical path. Across the source radiance levels, visual inspection of the difference between the fit determined attenuator transmittance and the one calculated with dn_{in} and dn_{out} through the calculated aperture spectral radiance ratio such as Eq. (7) showed that $a_1 dn$ is the worst performer. The goodness-of-fits showed that $a_1 dn\left(1 + c_2 dn + c_3 dn^2 + c_4 dn^3\right)$ performs the best. However, over the radiance slightly over the design specified maximum $L_{\max}$, the performance of $a_1 dn\left(1 + c_2 dn + c_3 dn^2 + c_4 dn^3\right)$ deteriorates quickly. This is due to the inaccuracy in the determined c_4 from errors in the input data. $a_1 dn\left(1 + c_2 dn + c_3 dn^2\right)$ yields

goodness-of-fit numbers which on average are better than any other polynomials considered in this study except $a_1 dn\left(1 + c_2 dn + c_3 dn^2 + c_4 dn^3\right)$, and over the spectral radiances larger than $L_{\max}$ this polynomial behaves nearly as good as over the range of $[L_{\min}, L_{\max}]$. Additionally, although $a_1 dn\left(1 + c_2 dn + c_3 dn^2 + c_4 dn^3\right)$ yields larger goodness-of-fit numbers than $a_1 dn\left(1 + c_2 dn + c_3 dn^2\right)$ for most bands, the numbers are very close in most cases; and for some bands $a_1 dn\left(1 + c_2 dn + c_3 dn^2\right)$ gives larger goodness-of-fit numbers than $a_1 dn\left(1 + c_2 dn + c_3 dn^2 + c_4 dn^3\right)$. Therefore, considering the performance over spectral radiance levels slightly larger than $L_{\max}$, $a_1 dn\left(1 + c_2 dn + c_3 dn^2\right)$ performs the best among the polynomials selected in this work. $a_1 dn\left(1 + c_2 dn\right)$ performs nearly as well as $a_1 dn\left(1 + c_2 dn + c_3 dn^2\right)$, except for the I3 band when *dn* is less than 600 or larger than 3200. In the future, we'd like to extend our analysis to the cases when the dual-gain bands are in low-gain stage and when the instrument was controlled at higher and lower temperatures.

ACKNOWLEDGMENTS

We thank Jeff McIntire, Thomas Schwarting, and Qiang Ji of Science Systems and Applications, Inc. for many useful discussions, and Hassan Oudrari of Science Systems and Applications, Inc. for useful comments on the manuscript.

REFERENCES

[1] X. Xiong, J. Sun, X. Xie, W. Barnes, and V. Salomonson, "On-Orbit Calibration and Performance of Aqua MODIS Reflective Solar Bands", *IEEE Trans. Geosci. Remote Sens.*, vol. 48, no. 1, pp. 535-546, Jan. 2010.

[2] X. Xiong, J. Sun, W. Barnes, and V. Salomonson, "Multiyear on-orbit calibration and performance of Terra MODIS reflective solar bands", *IEEE Trans. Geosci. Remote Sens.*, vol. 45, pp. 879-889, 2007.

[3] Joint Polar Satellite System (JPSS) VIIRS Radiometric Calibration Algorithm Theoretical Basis Document (ATBD); NASA Goddard Space Flight Center: Greenbelt, MD, USA, 2013.

[4] N. Lei, Z. Wang, and X. Xiong, "On-orbit Radiometric Calibration of Suomi NPP VIIRS Reflective Solar Bands through Observations of a Sunlit Solar Diffuser Panel", *IEEE Trans. Geosci. Remote Sens.*, vol. 53, pp. 5983-5990, 2015, DOI: 10.1109/TGRS.2015.2430814.

[5] Oudrari, H., McIntire, J., Xiong, X., Butler, J., Lee, S., Lei, N., Schwarting, T., and Sun, J., "Prelaunch Radiometric Characterization and Calibration of the S-NPP VIIRS Sensor", *IEEE Tran. Geosci. Remote Sens*, vol 53, pp. 2195-2210, 2015, DOI: 10.1109/TGRS.2014.2357678.

[6] N. Lei, K. Chiang, H. Oudrari, and X. Xiong, "A Maximum Likelihood approach to determine sensor radiometric response coefficients for NPP VIIRS reflective solar bands", *Proc. SPIE*, Vol. 8153, Paper 0J, 2011.

[7] C. B. Markwardt, "Non-Linear Least Squares Fitting in IDL with MPFIT," Proc. Astronomical Data Analysis Software and Systems XVIII, Quebec, Canada, in ASP Conference Series, Vol. 411, eds. D. Bohlender, P. Dowler & D. Durand (Astronomical Society of the Pacific: San Francisco), pp. 251-254, 2008.